

An $f/0.27$ High-Gain Lens Antenna for Ultrasmall Platforms at THz Frequencies

Van Berkel, Sven; Alonso-Delpino, Maria; Jung-Kubiak, Cecile; Chattopadhyay, Goutam

DOI

[10.1109/TTHZ.2023.3291450](https://doi.org/10.1109/TTHZ.2023.3291450)

Publication date

2023

Document Version

Final published version

Published in

IEEE Transactions on Terahertz Science and Technology

Citation (APA)

Van Berkel, S., Alonso-Delpino, M., Jung-Kubiak, C., & Chattopadhyay, G. (2023). An $f/0.27$ High-Gain Lens Antenna for Ultrasmall Platforms at THz Frequencies. *IEEE Transactions on Terahertz Science and Technology*, 13(5), 549-560. <https://doi.org/10.1109/TTHZ.2023.3291450>

Important note

To cite this publication, please use the final published version (if applicable). Please check the document version above.

Copyright

Other than for strictly personal use, it is not permitted to download, forward or distribute the text or part of it, without the consent of the author(s) and/or copyright holder(s), unless the work is under an open content license such as Creative Commons.

Takedown policy

Please contact us and provide details if you believe this document breaches copyrights. We will remove access to the work immediately and investigate your claim.





Green Open Access added to TU Delft Institutional Repository

'You share, we take care!' - Taverne project

<https://www.openaccess.nl/en/you-share-we-take-care>

Otherwise as indicated in the copyright section: the publisher is the copyright holder of this work and the author uses the Dutch legislation to make this work public.

An $f/0.27$ High-Gain Lens Antenna for Ultrasmall Platforms at THz Frequencies

Sven van Berkel , *Member, IEEE*, Maria Alonso-delPino , *Senior Member, IEEE*, Cecile Jung-Kubiak , *Senior Member, IEEE*, and Goutam Chattopadhyay , *Fellow, IEEE*

Abstract—The development of a low focal number and low-mass lens antenna is presented that enables terahertz spectroscopy applications on ultracompact platforms. The antenna operates efficiently over a 20% fractional bandwidth, from 450 to 550 GHz, with a gain of 50 dBi at 500 GHz. The antenna consists of a hyperbolic silicon lens that is placed in a record low focal number configuration ($f_{\#} = 0.27$) with respect to an advanced waveguide feed. An incident field-matching analysis is applied to investigate the optimal feed radiation pattern that maximizes the lens aperture efficiency, which would result in a 20% increase in aperture efficiency ($>80\%$) with respect to a standard open-ended waveguide ($<60\%$ aperture efficiency). A multilayer leaky-wave (LW) stratification is quasi-analytically optimized to approximate the optimal feeding pattern, resulting in a $>70\%$ lens aperture efficiency. An example LW stratification is synthesized using silicon micromachining technology and is fully characterized in combination with the dielectric lens.

Index Terms—Antenna, CubeSat, high gain, leaky-wave (LW) radiation, lens, low focal number, low profile, radiometry, SmallSat, spectroscopy, submillimeter wave, terahertz, waveguide (WG) feed.

I. INTRODUCTION

TERAHERTZ (THz) heterodyne spectroscopy instruments are extremely useful due to the abundance of strong molecular rotational and vibrational lines in this portion of the spectrum and the high spectral resolution that can be obtained [1]. In earth science, spectroscopy instruments provide valuable information about the composition of our atmosphere, e.g., in terms of air pollution, or water vapor content. Particularly, the abundance of water lines is of interest in planetary sciences, since

Manuscript received 28 April 2023; revised 16 June 2023; accepted 16 June 2023. Date of publication 11 July 2023; date of current version 5 September 2023. The research described herein was carried out at the Jet Propulsion Laboratory, California Institute of Technology, Pasadena, California, USA, under contract with National Aeronautics and Space Administration. Government sponsorship acknowledged (*Corresponding author: Sven van Berkel.*)

Sven van Berkel and Goutam Chattopadhyay are with the Submillimeter-Wave Advanced Technology Group, Jet Propulsion Laboratory, California Institute of Technology, Pasadena, CA 91109 USA (e-mail: sven.l.van.berkel@jpl.nasa.gov; goutam.chattopadhyay@jpl.nasa.gov).

Maria Alonso-delPino was with the Jet Propulsion Laboratory, California Institute of Technology, Pasadena, CA 91109 USA. She is now with the Terahertz Sensing Group, Delft University of Technology, 2628, CD Delft, The Netherlands (e-mail: m.alonsodelpino@tudelft.nl).

Cecile Jung-Kubiak is with the Advanced Microsensors and Microsystems Group, Jet Propulsion Laboratory, California Institute of Technology, Pasadena, CA 91109 USA (e-mail: cecile.d.jung@jpl.nasa.gov).

Color versions of one or more figures in this article are available at <https://doi.org/10.1109/TTHZ.2023.3291450>.

Digital Object Identifier 10.1109/TTHZ.2023.3291450

water is one of the key elements necessary to sustain life. The integration of a limb-sounding heterodyne THz spectrometer on an ultrasmall platform, such as a CubeSat or SmallSat, would provide an accessible and low-cost pathway to interplanetary space science. CubeSat instruments already have proven to be very successful at microwave frequencies, for the purpose of deep-space communications (Mars Cube One [2]) or low-earth-orbit (LEO) weather radar (RainCube [3]). Unfortunately, the heavy restrictions on volume (as small as $1U^1$) and mass (as light as 1.3 kg) make the design of the antenna front end very challenging [4]. Particularly, for spaceborne THz spectroscopy, a high-gain antenna (e.g., 50 dBi) is required to have sufficient sensitivity, while simultaneously a large frequency bandwidth will capture more molecular lines. In this article, we are targeting a 20% fractional frequency band, spanning from 450 to 550 GHz, to capture several water absorption lines simultaneously.

At millimeter-wave frequencies, low-profile antenna solutions, such as reflect [5], transmit [6], and antenna [7] arrays, have demonstrated antenna gains up to 43 dBi over a narrow bandwidth. High-gain deployable reflector antennas can currently only be realized efficiently up to Ka-band [8], as they become lossy at submillimeter-wave (submm-wave) frequencies since the surface roughness and accuracy requirements cannot be fulfilled. Similarly, attempts have been made with large deployable balloon reflectors [9], [10]. At submm-wave frequencies, a traditional metallic reflector can be used. The focal number of a reflector can be reduced significantly, but they have a high mass and suffer from blockage effects. Alternatively, elliptical integrated lens antennas at THz frequencies have been demonstrated with a high aperture efficiency [11], also over wide bandwidths [12], [13]. However, when a large radiating aperture is required (e.g., >70 mm antenna diameter for 50-dBi gain at 500 GHz), using elliptical lenses will result in an unpractically large volume of silicon. Thus, to the best of the authors' knowledge, no practical low-mass, low-profile, high-gain, and wideband antenna solution currently exist that would facilitate THz spectroscopy on ultrasmall platforms.

In an attempt to fill this antenna technology gap, we will use a free-standing hyperbolic silicon lens that is placed in a record low focal number configuration ($f_{\#} = 0.27$) with respect to a waveguide (WG) feed, as shown in Fig. 1. The efficient illumination of this lens is nontrivial because of its high numerical aperture, and thus, an advanced feeding structure is required.

¹1U is equivalent to a volume of $10\text{ cm} \times 10\text{ cm} \times 10\text{ cm}$.

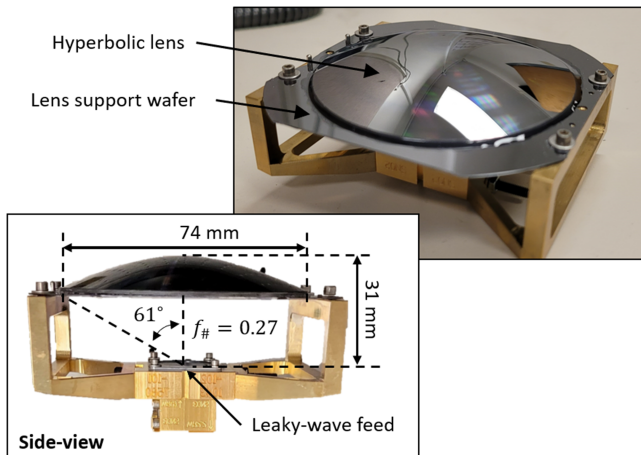


Fig. 1. Photographs of the fabricated low f -number lens antenna. Indicated are some critical dimensions and components.

The rest of this article is organized as follows. First, in Section II, we will investigate the ideal feed that maximizes the aperture efficiency by using an antenna-in-reception methodology. Subsequently, an attempt to synthesize this ideal feed is made by performing a numerical optimization of a multilayer leaky-wave (LW) stratification. Both a narrowband and wideband optimization is presented. Then, in Section III, we present the fabrication of an example LW stratification and assembly of the lens antenna. Measurements of the feed and lens antenna are presented in Section IV. A standard near-to-far-field (NF-to-FF) transformation is applied to estimate the far-field performance of the lens antenna. Finally, Section V concludes this article.

II. LENS ANTENNA FEED DESIGN

Consider a free-standing silicon lens, with a hyperbolic top surface and flat bottom surface. Silicon is chosen as the lens material to minimize the lens thickness and dielectric losses [high-resistivity floating-zone silicon with resistivity $\rho > 10 \text{ k}\Omega\cdot\text{cm}$ ($\equiv \tan \delta < 3.4 \times 10^{-5}$) and relative permittivity $\epsilon_r = 11.9$ is assumed]. Throughout this article, we will consider a Parylene-C antireflection (AR) coating ($\epsilon_r = 2.62$ and $\tan \delta = 0$ is assumed) deposited on the hyperbolic top surface and an ideal quarter-wavelength transformer ($\epsilon_r = 3.45$) on the flat bottom surface. As will be shown in Section III, this ideal quarter-wavelength transformer can be silicon micromachined in the lens support wafer on which the lens will be glued, as indicated in Fig. 1 and later elaborated on in Fig. 8. The diameter of the lens, 74 mm, follows from the desired antenna gain of 50 dBi at 500 GHz, allowing for a lens aperture efficiency of 65%. By using standard ray tracing techniques, the hyperbolic lens surface, in terms of radius of curvature and conic constant, is optimized as a function of the lens truncation angle, θ_0 . The resulting antenna height h_{ant} , defined as the sum of the focal distance and lens thickness, is calculated and is shown by the blue curve in Fig. 2. As a reference, the antenna height for a fused silica lens and plastic lens are also shown by the red and yellow curves, respectively. It is clear that silicon is the preferred lens

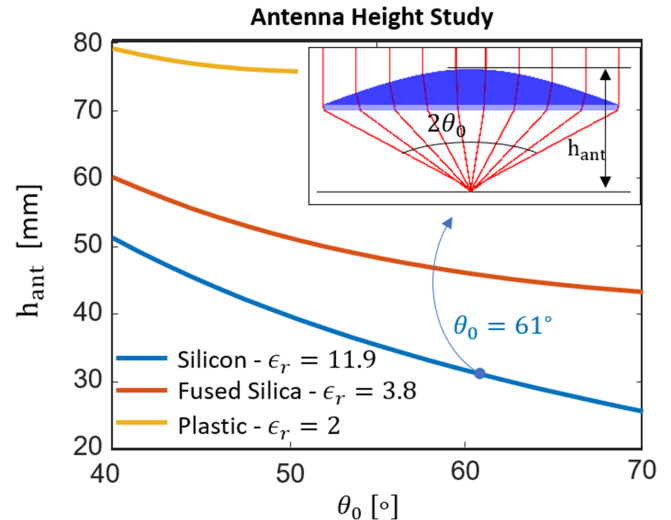


Fig. 2. Antenna height study as function of lens truncation angle for a $D_l = 74.3 \text{ mm}$ diameter lens. Investigated materials are silicon (blue), fused silica (red), and plastic (yellow). A wide truncation angle of 61° is chosen to minimize the antenna profile.

material for low focal number lenses. An antenna height close to 3 cm is targeted such that the antenna consumes a volume much smaller than 1U, leaving enough space for other components of the spacecraft. Therefore, a wide lens truncation angle of $\theta_0 = 61^\circ$ is chosen. The resulting lens antenna configuration, shown in Fig. 1, has a record low focal number $f_{\#} = F/D = 0.27$, where $F = 20.2 \text{ mm}$ is the focal distance and $D = 74 \text{ mm}$ is the diameter of the lens. The lens is approximately 10.4 mm thick at the center. The lens edge is chosen to be 1.45 mm thick, of which $450 \mu\text{m}$ will be attributed to the lens support wafer indicated in Fig. 1. The chosen lens truncation angle could significantly limit the lens aperture efficiency that can be realized. Aperture efficiencies higher than 90% can be achieved for smaller truncation angles, by simply using standard horns or open-ended waveguide (OEWG) feeds. Lens antennas with large lens truncation angles become highly underilluminated using those feeds. How to illuminate this lens efficiently will be the discussion of the remaining part of this section.

A. Low- $f_{\#}$ Lens Antenna Geometrical Optics (GO) Analysis

It is well known that the aperture efficiency of a quasi-optical system is maximized when the field radiated by the antenna feed, when evaluated in transmission, is a conjugate match to the inward incident field of the quasi-optical system evaluated in reception. This field-matching technique was first developed for reflector feeds [14] and later generalized in [15] and [16] using the equivalence theorem. In [17], the incident field is studied, using GO methods, for plastic and silicon elliptical lenses, showing the need for cosine-shaped feed patterns for low-permittivity elliptical lenses and square-shaped, *top-hat*, feed patterns for silicon lenses, such as the multimode LW lens antenna feeds presented in [12].

Here, we study the inward incident field of the considered low- $f_{\#}$ hyperbolic silicon lens. As is illustrated by the inset

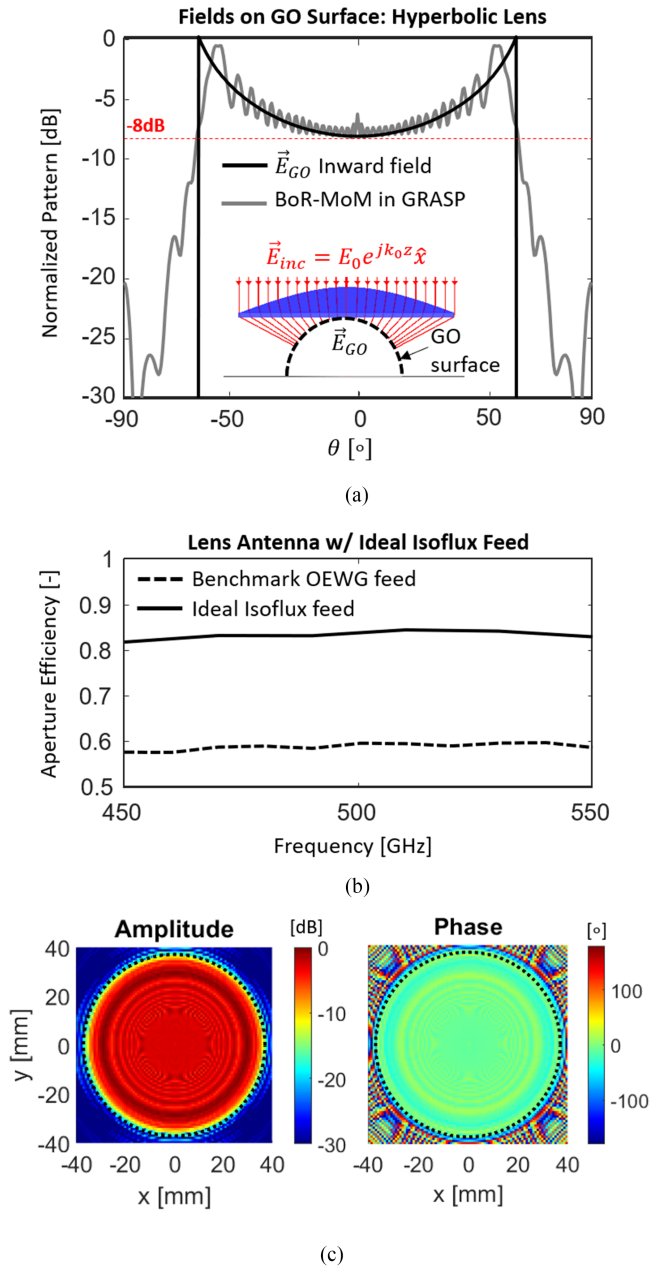


Fig. 3. Lens antenna study with ideal isoflux feed. (a) Inward incident field (E-plane) on the GO surface, evaluated with the GO method (black) compared with a simulated BoR-MoM in GRASP (gray). The inset shows the definition of the GO surface. (b) Simulated lens aperture efficiency with the ideal isoflux feed (solid) compared with a benchmark OEWG feed (dashed). (c) Near-field distributions at 500 GHz for the isoflux feed, simulated in a plane 10 mm above the lens surface in GRASP.

of Fig. 3(a), the hyperbolic lens is illuminated by a uniform, single-polarized, plane wave, and the field is propagated using GO methods to a hemisphere centered at the focal point of the lens. The resulting inward incident field \vec{E}_{GO} in the E-plane is shown by the black curve in Fig. 3(a) and resembles an *isoflux*-shaped pattern with a maximum intensity at the lens edge and a low, -8 dB, normalized intensity at broadside. The isoflux shape is mainly caused by the power spreading factor (sometimes called space taper). The inward field is rotationally

symmetric since matching layers are considered in the field evaluation. The inward incident field is also simulated using a bodies-of-revolution method of moments (BoR-MoM) in commercial software TICRA GRASP and is shown by the gray curve. The oscillations that can be seen in the BoR-MoM simulation are due to multiple reflections in the lens and diffraction occurring at the lens edges, which are not included in the GO-method field evaluation.

In order to see what lens aperture efficiency can be achieved when the lens is illuminated by an isoflux feed pattern, we have performed a BoR-MoM simulation in TICRA GRASP using the GO inward incident field [black curve in Fig. 3(a)] imported as a tabulated feed. The result, shown by the solid curve in Fig. 3(b), is an aperture efficiency higher than 80% over the full bandwidth. This is an increase of more than 20% with respect to a benchmark OEWG feed, indicated by the dashed curve. In this benchmark simulation, the diameter of the OEWG, D_{WG} , is chosen to be close to cutoff, $D_{WG} = 2\lambda_0/3$, where λ_0 is the free-space wavelength at 500 GHz, to illuminate the lens more uniformly at the cost of a slight pattern asymmetry, increased spillover losses, and increased return loss. A slight improvement in aperture efficiency could be achieved when applying annular corrugations around the WG aperture to make the pattern more symmetric [18], [19], [20].

The simulated amplitude and phase of the lens near-field distribution, when illuminated with the ideal isoflux pattern and evaluated 10 mm above the lens surface, are shown in Fig. 3(c). Indicated with the dotted black circle is the lens diameter. It is evident that the field is highly uniform in amplitude and phase. As expected from the simulation in Fig. 3(a), some oscillations can be identified in the near-field distribution due to multiple reflections occurring in the lens. Those reflections become more profound for larger illumination angles as the matching layers become less efficient.

B. Synthesized Multilayer LW Feed

The analysis of the inward incident field in the previous section showed that an isoflux-shaped feed pattern is desired to maximize the lens aperture efficiency. Such a feeding pattern is also desired for global earth coverage with LEO satellites to achieve uniform power density over the visible portion of the earth or to compensate for the power spreading factor in low- $f_{\#}$ reflector antennas [21]. The proposed low-profile isoflux antennas at microwave frequencies are, for example, based on metasurfaces [22], [23], dielectric-loaded patch antennas [24], or concentric ring antenna arrays [25]. WG-based solutions use annular corrugations [26] or LW beam-shaping phenomena [27], [28], which is the solution used in this article. The solution is based on a multilayer LW stratification, excited by an OEWG. More layers give a higher beam-shaping flexibility but increases fabrication complexity. A four-layer LW stratification is optimized as a function of layer height, h_i , and relative permittivity, ϵ_i , for $i = 1$ to 4, as illustrated in Fig. 4. The diameter of the input WG is fixed to $D_{WG} = \lambda_0 = 600 \mu\text{m}$. This diameter is well above cutoff to minimize the return loss but still small enough to allow for wide-angle beam shaping with LWs. The far-field

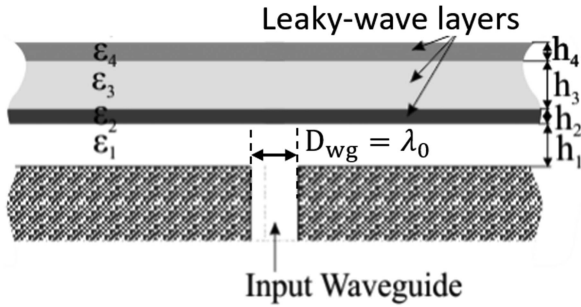


Fig. 4. Feeding structure to be optimized, consisting of a four-layer LW stratification excited by an open-ended circular WG.

TABLE I
OPTIMIZED LW STRATIFICATIONS FROM FIG. 5

Layer i	Narrowband Optimization			Wideband Optimization		
	ϵ_{ri}	h_i/λ_0	$h_i/\mu\text{m}$	ϵ_{ri}	h_i/λ_0	$h_i/\mu\text{m}$
1	1.4	0.368	221	1	0.748	449
2	1.5	0.200	120	11.9	0.111	66
3	12.5	0.058	35	4.1	0.101	61
4	2.4	0.192	115	—	—	—

radiation pattern of the LW feed, \vec{E}_a^{Tx} , is computed using the asymptotic far-field approximation and the Green's functions for stratified media [29]. A particle swarm optimization (PSO) is then applied to maximize the field matching with the inward incident GO field, \vec{E}_{GO} , from Fig. 3(a). More specifically, the algorithm maximizes an approximation of the lens aperture efficiency, η_{ape} , [15], [17]:

$$\eta_{\text{ape}} \approx \frac{|\frac{2}{\zeta_0} \int_0^{2\pi} \int_0^{\pi/2} (\vec{E}_a^{\text{Tx}} \cdot \vec{E}_{\text{GO}}) R_{\text{GO}}^2 \sin \theta d\theta d\phi|^2}{16 P_{\text{rad}}^{\text{Tx}} P_{\text{inc}}^{\text{PW}}} \quad (1)$$

where R_{GO} is the radius of the equivalent GO surface on which the fields are evaluated and ζ_0 is the free-space intrinsic impedance. $P_{\text{rad}}^{\text{Tx}}$ and $P_{\text{inc}}^{\text{PW}}$ are, respectively, the power radiated by the feed evaluated in transmission and power incident in the plane wave.

1) *Narrowband Optimization*: LW phenomena are intrinsically dispersive and the required bandwidth directly affects the optimization results. In order to investigate the full potential of using a multilayer LW stratification to maximize the lens aperture efficiency, an optimization is first done over a narrowband from 480 to 520 GHz (8% fractional bandwidth). The PSO search space for the relative permittivity of each layer is defined from 1 to 16.25, allowing for germanium substrates. The search space for layer height ranges from 0.01 to $1\lambda_0$. The lens aperture efficiency (1) of each configuration is evaluated for five equally spaced frequency points. The inverse of the frequency-averaged aperture efficiency defines the cost function that is minimized by the PSO algorithm. The optimized dielectric layer properties are shown in Table I. The first two layers have an optimized permittivity close to the one of free space, whereas the third layer has an optimized permittivity slightly larger than the one of silicon. This stratification leads to a lens aperture efficiency between 73% and 78% over the optimization bandwidth, as shown by the blue curve in Fig. 5(a). There, the approximated

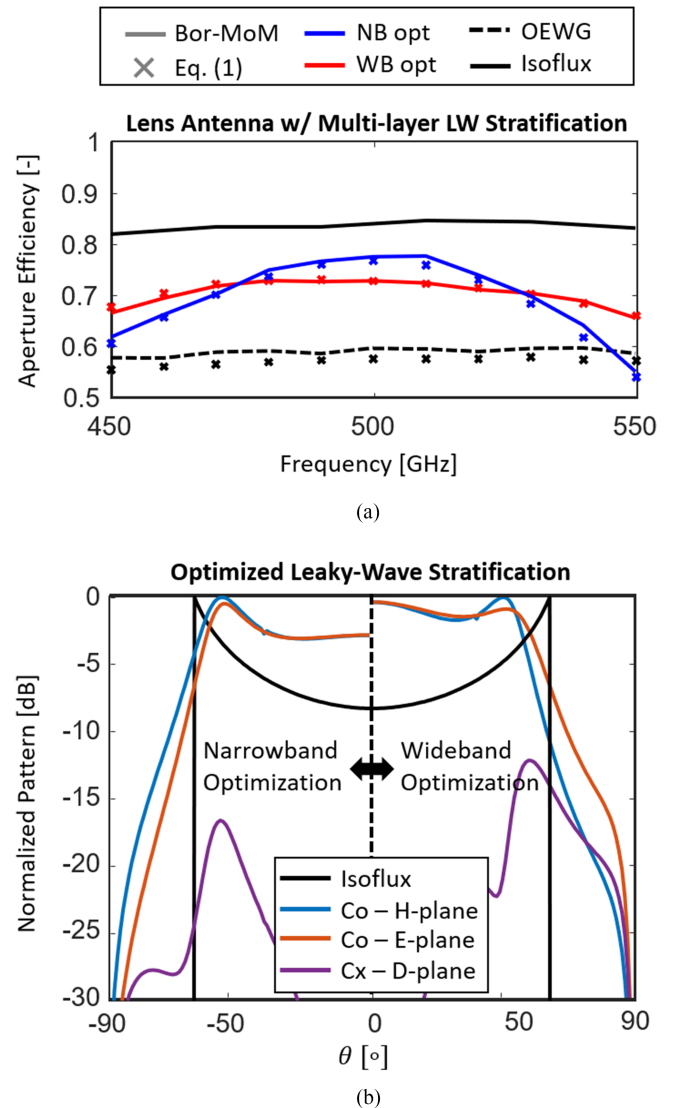


Fig. 5. Lens antenna performance with optimized multilayer LW feeds. (a) Simulated lens aperture efficiency for optimized narrowband (blue, NB opt) and wideband (red, WB opt) stratification. Compared are the aperture efficiencies approximated by (1) (crosses) and as simulated with a BoR-MoM in TICRA CHAMP 3D (solid lines). (b) Feed radiation pattern at 500 GHz for the narrowband and wideband optimization.

lens aperture efficiency as optimized by using the field-matching technique (1) is shown by the blue crosses and is compared with a BoR-MoM simulation using TICRA CHAMP 3D (solid), illustrating the validity of the quasi-analytical optimization procedure. The radiation pattern of the LW feed at 500 GHz is shown by the left-hand side of Fig. 5(b) and is compared with the inward incident GO field (black curve). It is clear that the isoflux pattern is only partly synthesized with a -3 dB radiation intensity at broadside, and consequently, the optimal 84% lens aperture efficiency of the isoflux feed from Section II-A is not achieved. Yet, a significant improvement with respect to the OEWG feed is achieved, as is evident from the aperture efficiency shown in Fig. 5(a).

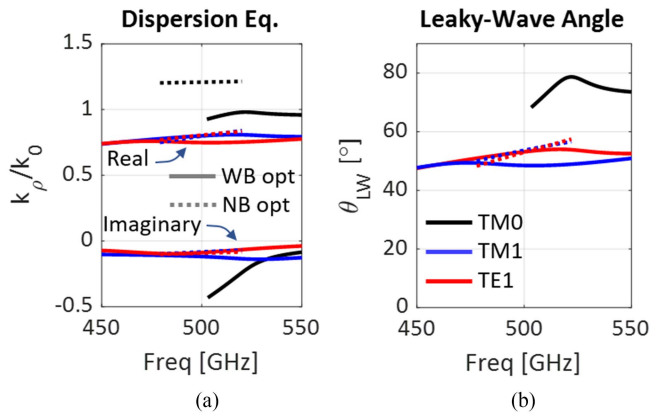


Fig. 6. LW and SFW modes supported in the optimized narrowband (NB, dotted lines) and wideband (WB, solid lines) stratifications. (a) Solution to the dispersion equation, showing the complex propagation constants of the TM_0 (black), TM_1 (blue), and TE_1 (red) LW/SFW modes. (b) Pointing angles of the supported LW modes.

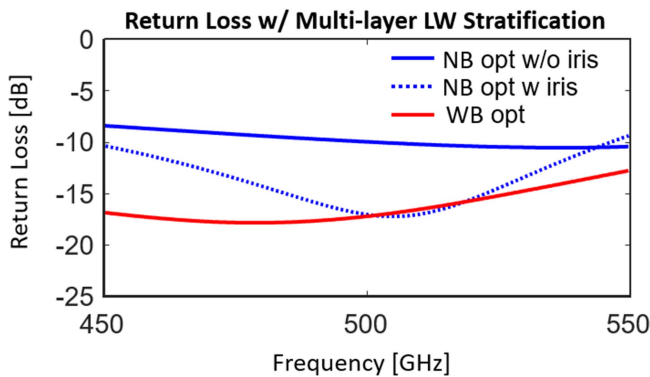


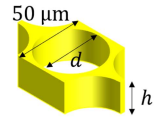
Fig. 7. Simulated return loss of the optimized LW feeds. The return loss for the narrowband (blue) feed is shown with (dashed) and without (solid) a double-slot iris.

The supported LW modes are analyzed by finding the poles of the equivalent transmission line circuit model of the stratification. The solution to this dispersion equation of the optimized stratification is shown in Fig. 6(a) and (b) with the dotted lines. The fundamental TM_1/TE_1 LW mode pair (dotted red and blue) has approximately the same complex propagation constant, which translates to a large LW pointing angle of approximately 53° and a normalized attenuation constant of $0.1k_0$, where k_0 is the free-space wavenumber. A TM_0 surface-wave (SFW) mode (dotted black) is supported with real-valued propagation constant $1.2k_0$. To minimize the TM_0 SFW mode excitation, a double-slot iris can be used [30]. A double-slot iris will also improve the return loss, as shown in Fig. 7, with a simulation performed in CST Microwave Studio.

2) *Wideband Optimization*: Next, a stratification is optimized over the targeted wide frequency bandwidth, i.e., from 450 to 550 GHz (20% fractional bandwidth). Moreover, the maximum relative permittivity of each layer is now restricted to $\epsilon_r = 11.9$ since the stratification will be fabricated using silicon micromachining technology, as will be discussed in Section III.

TABLE II
SYNTHESIZED DIELECTRIC LAYERS IN SILICON

i	ϵ_{ri}	h_i [μm]	Porosity [%]	d_i [μm]
1	1	450	100	N/A
2	5.8	71	41	34
3	2.4	37	79	47
4	3.1	46	69	44
AR	3.5	81	65	42



The resulting stratification parameters are also summarized in Table I, and the lens aperture efficiency (1) and feed radiation pattern are shown in Fig. 5(a) and (b) respectively. The pattern now resembles more a top-hat shape, leading to a slightly lower lens aperture efficiency, between 66% and 73%, that is, however, constant over a wideband. The spillover and reflection losses are simulated to be less than 10%. Only three dielectric layers are required in this stratification, easing fabrication complexity. The LW modes are summarized in Fig. 6 by the solid lines. The undesired TM_0 LW mode is highly attenuating, and the TM_1/TE_1 LW mode pair is stable and pointing approximately at a 50° angle. The feed is well matched, as shown by the red curve in Fig. 7.

III. FABRICATED LW FEED AND LENS ANTENNA ASSEMBLY

We have fabricated a demonstrator lens antenna, of which an exploded view is shown in Fig. 8. For this demonstrator, a slightly different LW stratification was fabricated. The fabricated stratification was the result of an earlier optimization implementation that targeted a more uniform illumination of the lens (i.e., a *top-hat* distribution), rather than the discussed *isoflux* shape from the previous section. The synthesized relative permittivity of the four layers ($i = 1, \dots, 4$) of the fabricated multilayer LW stratification are summarized in Table II. The LW properties of the fabricated feed are summarized in Fig. 9, indicating the existence of a slowly attenuating TM_0 LW mode pointing at a large $>80^\circ$ angle and the desired TM_1/TE_1 LW mode pair pointing at a 50° angle. The permittivity of each layer is synthesized by perforating silicon with holes in a $50 \mu\text{m}$ -periodicity hexagonal grid. The porosity of the silicon, also summarized in Table II, is calculated based on the theory presented in [31] and directly defines the diameter d_i of the perforations. The layers are micromachined, using deep-reactive ion etching (DRIE) techniques, in two silicon-on-insulator (SOI) wafers, which are then attached on a WG block using plastic screws, as illustrated in Fig. 8. Wafer #1 is $450 + 71 \mu\text{m}$ thick and contains layers $i = 1$ and 2. Wafer #2 is $450 + 83 \mu\text{m}$ thick and contains layers 3 and 4. The SOI wafers are custom made at WaferPro and UltraSil, with device thicknesses and resistivity that match with the optimized design. For multiple-step etching, we have developed a process presented in [32], where silicon dioxide (SiO_2) is used as the primary mask. It is pre-etched in step increments to match both the selectivity $\text{SiO}_2 : \text{Si}$ on the DRIE and the number of steps on the design. The diameter of the LW cavity, 20 mm, is chosen to be much larger than the -20 dB field decay of the main LW modes, which can be derived from the imaginary part of the complex propagation constant in Fig. 9(a). The hole diameter of the perforations is

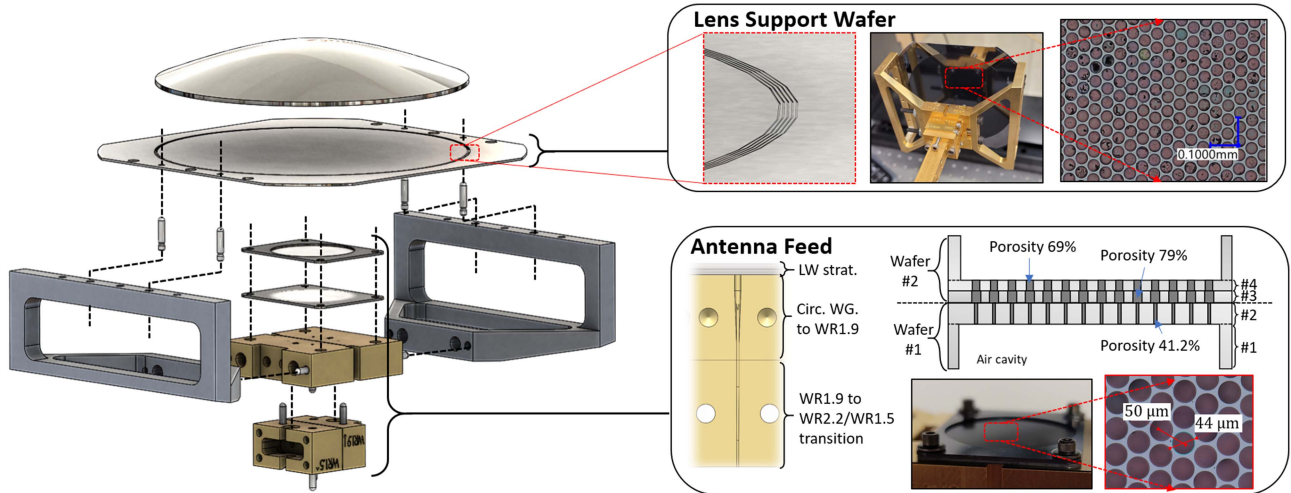


Fig. 8. Exploded view of the low- $f_{\#}$ lens antenna. The lens support wafer contains lens alignment rings on the top and a quarter-wavelength AR layer on the bottom. The antenna feed is a multilayer LW stratification that machined in two SOI wafers. Two WG blocks are not considered to be part of the antenna but provide transitions to facilitate the measurements.

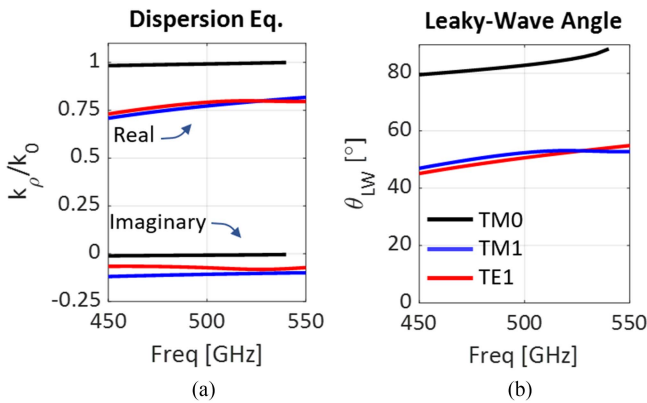


Fig. 9. LW modes supported in the fabricated LW stratification. (a) Solution to the dispersion equation, showing the complex propagation constants of the TM_0 (black), TM_1 (blue), and TE_1 (red) modes. (b) Pointing angles of the supported LW modes.

machined with a tolerance of approximately $1 \mu\text{m}$, whereas the periodicity is exact as it is set relative to the whole wafer. Using the theory in [31], a $\pm 1 \mu\text{m}$ error in diameter is estimated to result in an error in relative permittivity up to $\Delta\epsilon_{r,i} = \pm 0.27$. In simulation, it is verified that an error in layer permittivity results in a graceful degradation of antenna performance. The WG block is fabricated in gold-plated aluminum using split-block technology and forms a transition from the open-ended circular WG to a WR-1.9 rectangular WG definition. A second WG block forms an additional transition to either the WR-2.2 or WR-1.5 rectangular WG definition, since those are the vector network analyzer (VNA) frequency extenders that were available to us. The WG blocks are, however, not considered to be part of the antenna since they merely facilitate the measurement. In an actual heterodyne THz spectroscopy system, the mixers are placed close to the WG aperture to minimize ohmic dissipation losses.

The hyperbolic silicon lens was machined using diamond turning and then provided with a Parylene-C AR coating on the hyperbolic top surface. A nominal thickness of $93 \mu\text{m}$ was targeted, which can be typically achieved with a tolerance better than 20%. The lens was subsequently glued on top of a lens support wafer. This SOI wafer is $450 \mu\text{m} + 81 \mu\text{m}$ thick, of which $450 \mu\text{m}$ is used as lens extension and $81 \mu\text{m}$ will be machined into the AR layer. As is highlighted in Fig. 8, shallow lens alignment rings are etched in a $50\text{-}\mu\text{m}$ periodicity on the top surface of the lens support wafer to allow for a visual alignment of the lens before applying commercially available Loctite superglue. The bottom side of the lens support wafer contains the quarter-wavelength AR layer. Details of the AR layer are also summarized Table II. The lens support wafer is fixated to the WG feed block using aluminum support brackets, and a good alignment between the feed and lens is assured by using dowel pins and holes.

IV. MEASUREMENTS

In this section, the LW lens antenna will be fully characterized in terms of feed patterns, return loss, far-field lens patterns, and efficiency. The measurement setup to evaluate the multilayer LW feed is shown in Fig. 10, whereas the complex near field of the lens will be evaluated using the setup shown in Fig. 11. The far-field patterns will be extracted from an NF-to-FF transformation using the measured near field, whereas the efficiency is evaluated by using a near-field self-coupling experiment and de-embedding of the WG transitions.

A. Multilayer LW Feed Measurements

First, the feed is attached to a two-axis gimbal stage that scans the two main planes of the feed, as shown in Fig. 10. The feed is measured both in the WR-2.2 and WR-1.5 frequency bands using frequency extenders from Virginia Diodes Inc. (VDI), connected using the appropriate WG transition to WR-1.9, as shown in

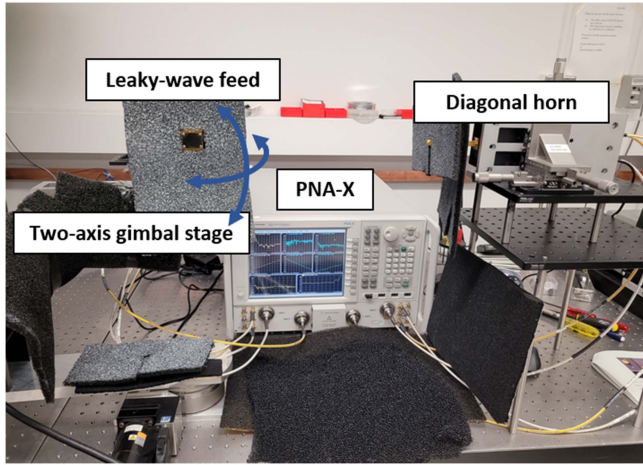


Fig. 10. Measurement setup for the LW feed analysis.

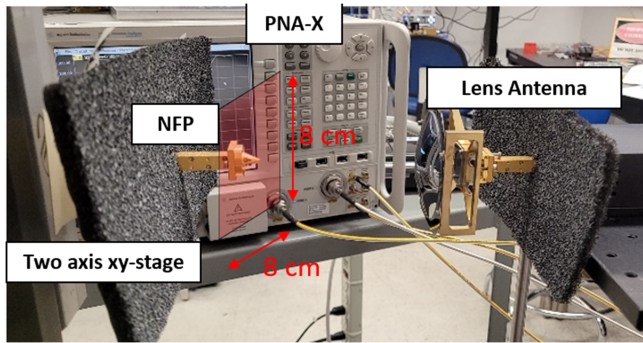


Fig. 11. Measurement setup to evaluate the complex near field radiated by the lens antenna. The NFP performs a planar scan using a two-axis xy stage.

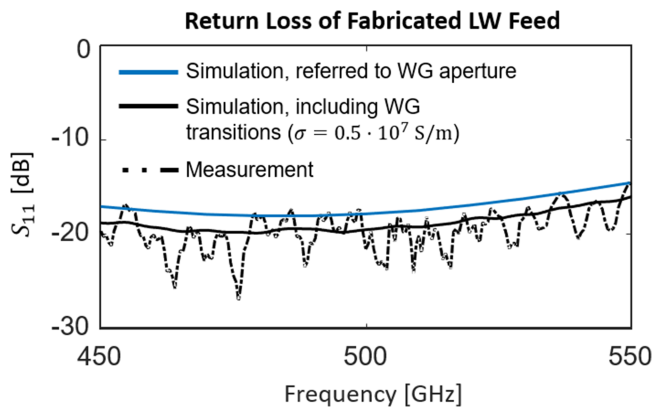


Fig. 12. Measured return loss (dashed black), compared with simulation with (solid black) and without (solid blue) lossy WG blocks.

Fig. 8. A standard VDI diagonal horn is used as measurement antenna, and a Keysight PNA-X is used as VNA.

A one-port calibration is performed to measure the return loss of the feed. The measured and simulated return loss are shown in Fig. 12 by the dashed and solid black lines, respectively. The simulation assumes a WG wall conductivity of $\sigma = 0.5 \times 10^7$ S/m, as will be extracted from measurements presented in

the next section. As a reference, the simulated return loss seen from the circular WG aperture is shown by the solid blue curve. The feed is well matched with a return loss well below $S_{11} < -15$ dB over the entire bandwidth.

The measured normalized feed patterns are shown by the dashed lines in Fig. 13 and correspond well with the simulated patterns (solid) evaluated with the asymptotic far-field approximation. When comparing the patterns of the fabricated stratification in Fig. 13, with the simulated pattern of the optimized wideband stratification from Fig. 5, we can identify a larger contribution of the TM_0 LW mode, as was predicted by the LW mode analysis presented in Fig. 9. Although the impact of the undesired TM_0 LW mode is small, it may be noted that this mode is not excited with the optimized wideband stratification, as proposed in Section II-B.

B. Lens Antenna Measurements

The near-field measurement setup to evaluate the lens antenna performance is shown in Fig. 11. The lens antenna is evaluated in the near field since the Fraunhofer distance is larger than $r_{FF} = 2D^2/\lambda_0 > 15$ m for the considered lens aperture, making far-field measurement impractical. Instead, a planar $8\text{ cm} \times 8\text{ cm}$ scan is performed on a two-axis xy -stage using a near-field probe (NFP) by Anterol, in close proximity of the lens aperture. The measurement scanning step is $500\ \mu\text{m}$ (slightly undersampled). The resulting complex near-field distributions, S_{12} , are shown in Fig. 14 at the frequencies 450, 500, and 550 GHz in terms of amplitude and phase. A black dotted circle illustrates the diameter of the lens. The measured phase distribution that is shown in Fig. 14 has been corrected for the linear phase shift distribution embedded in the measurement due to any misalignment between the measurement plane and the antenna plane. The required linear phase-shift correction is derived from an NF-to-FF transformation of the complex near field and by observing the scanning direction of the resulting far-field beam.² Note that such correction does not change the shape or quality of the beam patterns but merely centers the pattern at a broadside direction. Any pattern degradation due to coma phase contributions, as a result of feed misalignment with respect to the lens focus, is still preserved in the corrected measurements. One can appreciate the flat phase front distributed over the entire lens aperture, as shown in Fig. 14(d)–(f). Moreover, the amplitude is relatively uniform in the center of the lens but is tapered at the edges. A more uniform distribution can be achieved if the lens is illuminated by an isoflux pattern, as discussed in Section II-A.

The far-field beam-patterns, resulting from the NF-to-FF transformation of the complex S_{12} distributions in Fig. 14, are shown in Fig. 15 at the frequencies 450, 500, and 550 GHz. The 2-D patterns are shown in Fig. 15(a)–(c) in uv -coordinates, whereas the main cuts are shown in Fig. 15(d)–(f) by the dashed lines. The cuts are compared with the beam patterns as simulated with the BoR-MoM (solid lines). The beams are symmetric and have a high Gaussicity. The Gaussicity and main beam efficiency, evaluated from the 2-D patterns, are shown in Fig. 16.

²It was found that $\theta_s = 0.25^\circ$ and $\phi_s = 124^\circ$.

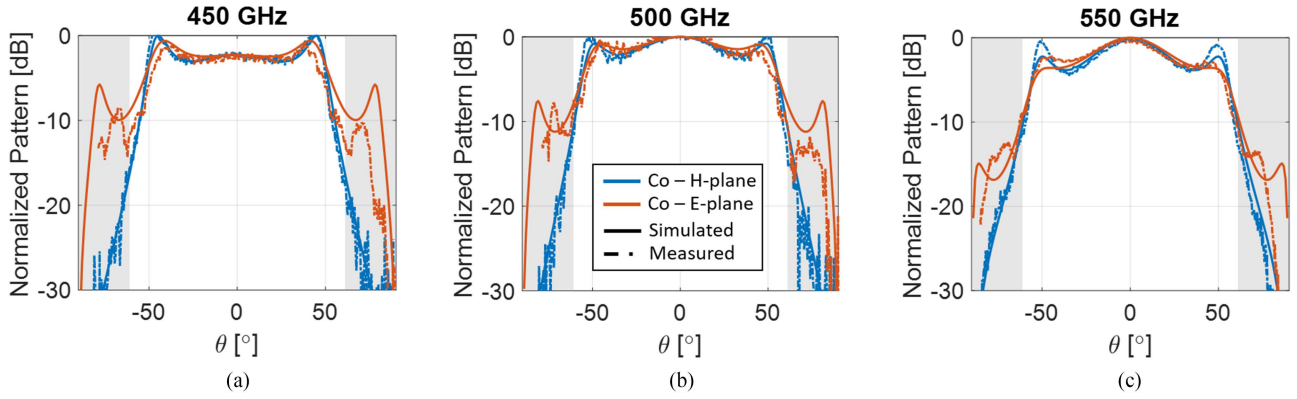


Fig. 13. Measured LW feed patterns (dashed), compared with simulations (solid). Shown are the H-plane (blue) and E-plane (red) cuts at (a) 450 GHz, (b) 500 GHz, and (c) 550 GHz.

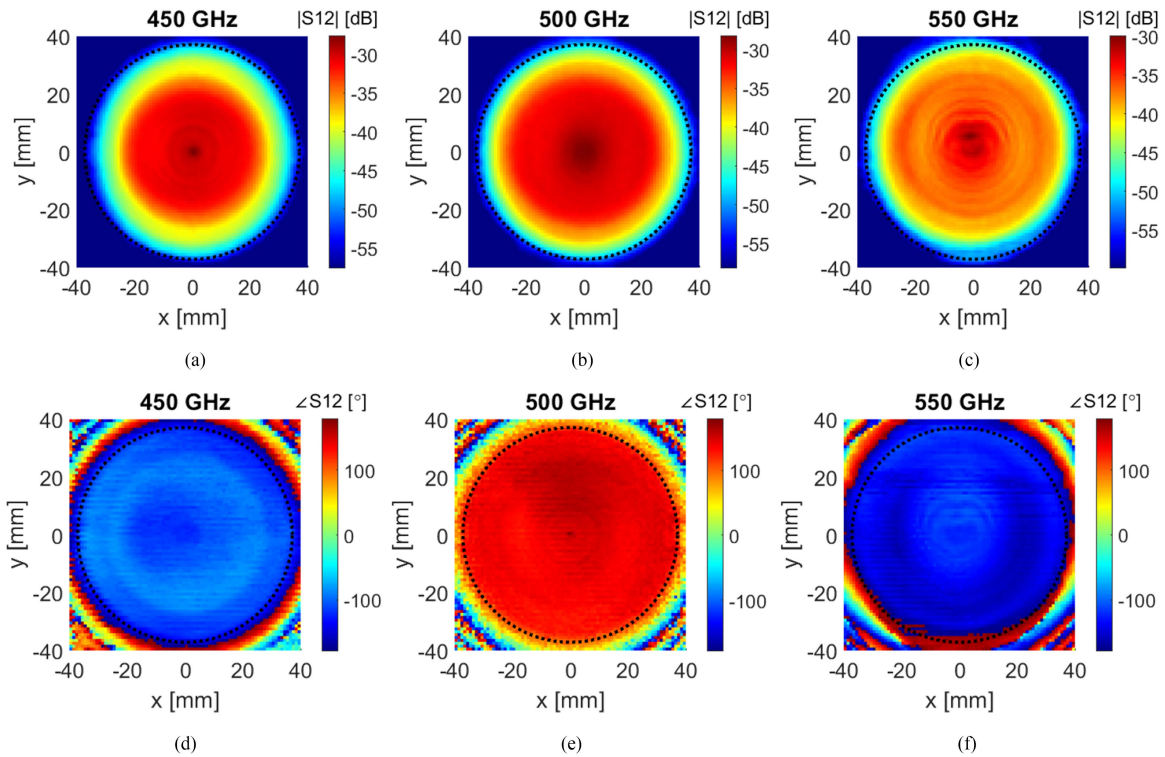


Fig. 14. Measured near-field distribution of lens antenna. (a)–(c) Amplitude of S_{12} in dB. (d)–(f) Phase of S_{12} in degrees. Shown are results at 450 GHz (a), (d), 500 GHz (b), (e), and 550 GHz (c), (f). The black dotted ring indicates the diameter of the hyperbolic lens.

The calculation does not include power that is in spillover of the lens or reflected on the lens surface, since this power is not captured by the near-field measurement.

The aperture efficiency of the lens antenna is extracted from the measured near field combined with two additional coupling measurements that are depicted in Fig. 17. In Fig. 17(a), a near-field self-coupling experiment is shown. In this experiment, two identical lens antennas are facing each other in close proximity, and the transmission parameter is defined as the near-field self-coupling efficiency, $|S_{12}|^2 = \eta_{sc}$. This efficiency term will include the radiation efficiency due to ohmic dissipation in the WG blocks (η_{rad}) and all relevant aperture efficiency (η_{ape}) terms, except for the amplitude tapering efficiency (η_{tap}^{ampl}), assuming

that the two antennas shown in Fig. 17(a) have the same amplitude of their near-field distribution [33]

$$\eta_{sc} = \left(\frac{\eta_{ape}}{\eta_{tap}^{ampl}} \eta_{rad} \right)^2. \quad (2)$$

The measured near-field self-coupling efficiency is shown by the gray dash-dotted curve in Fig. 18. Shown by the black dash-dotted curve is the same, but time-gated, measurement in order to mitigate the effect of multiple reflections between the two lens antennas. Note that discrete step at 500 GHz is the result of switching the frequency extension heads and WG transitions from WR-2.2 to the WR-1.5 definition.

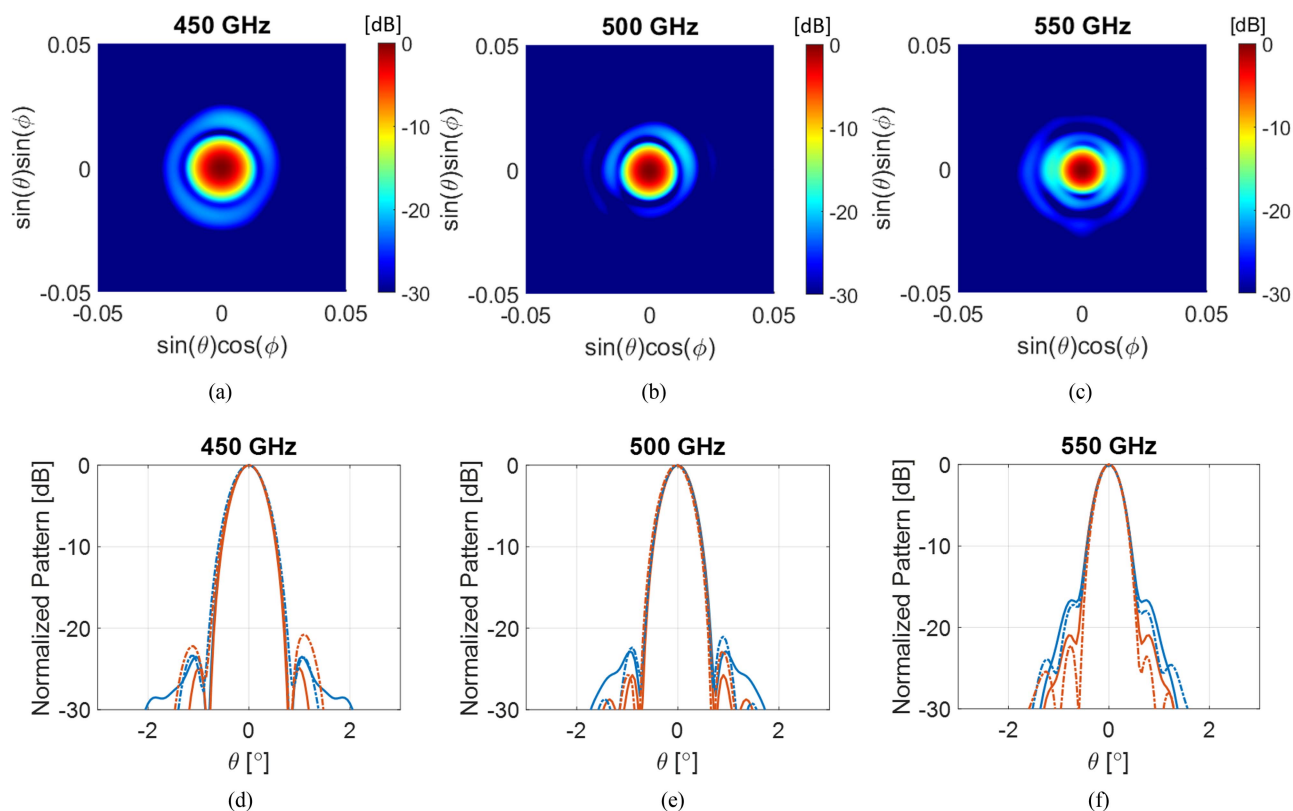


Fig. 15. Far-field lens patterns derived from the measured near field shown in Fig. 14. (a)–(c) 2-D patterns in the uv -coordinates. (d)–(f) Main plane cuts, E-plane (red), and H-plane (blue). Shown are simulated values (solid curves) and the results of the measured NF-to-FF transformation (dashed curves). Results are shown for frequencies 450 GHz (a), (d), 500 GHz (b), (e), and 550 GHz (c), (f).

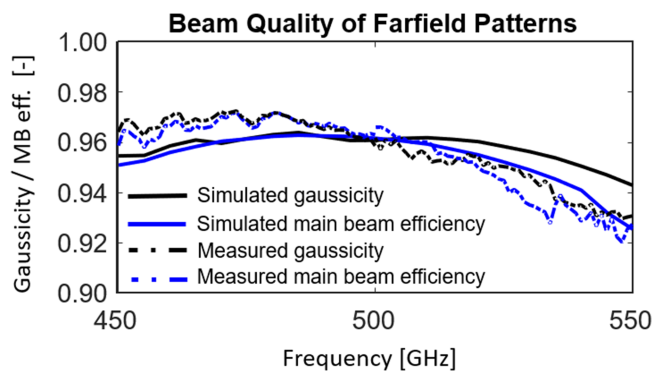


Fig. 16. Beam quality of far-field patterns in terms of Gaussiaicity (black curves) and main beam efficiency (blue curves). The simulations (solid curves) are compared with the quantities derived from the measured NF-to-FF transformation (dash-dotted curves).

A second coupling experiment is illustrated in Fig. 17(b) and measures the transmission through two back-to-back WG transitions. This measurement is used to derive the conductivity of the gold-plated aluminum blocks. This measurement is shown in Fig. 18 by the red dash-dotted curves. This measurement corresponds well with the simulated transmission of the WG blocks, in CST Microwave Studio, when the WG wall conductivity is defined as $\sigma = 0.5 \times 10^7$ S/m. The simulated near-field

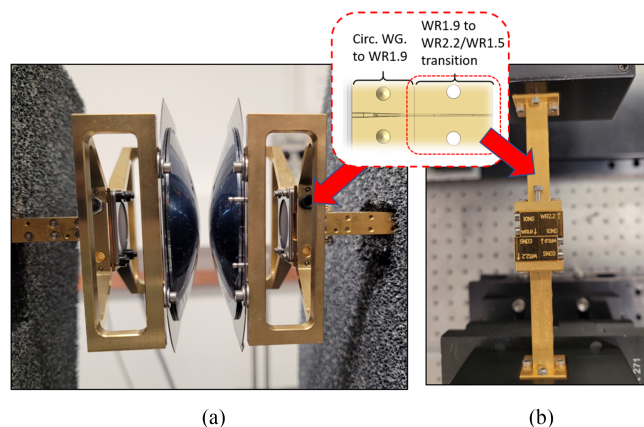


Fig. 17. Measurement setup to evaluate the efficiency of the lens antenna. (a) Near-field self-coupling experiment. (b) Calibration measurement to extract WG conductivity. (Inset) Schematic of the WG blocks used in the measurements.

self-coupling efficiency (2), simulated using the extracted WG block conductivity, is shown by the solid black line in Fig. 18. Overall, the simulation corresponds well with the self-coupling measurement. The measured self-coupling is slightly lower at the edges of the frequency band. It may be noted that some discrepancy between simulation and the measurement might be due to a misalignment between the two antennas. If the

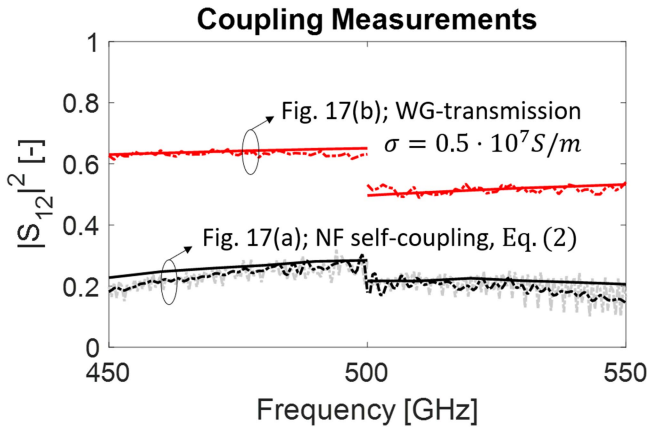
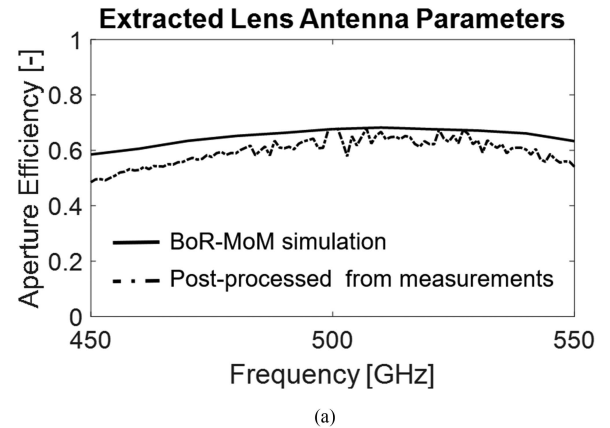


Fig. 18. Results of the near-field self-coupling measurements [from Fig. 17(a)]: Raw NF self-coupling efficiency (gray dash-dotted), time-gated NF self-coupling efficiency (black dash-dotted), and simulation (black solid). Also shown are the results WG block transmission measurements from Fig. 17(b) (red curves).

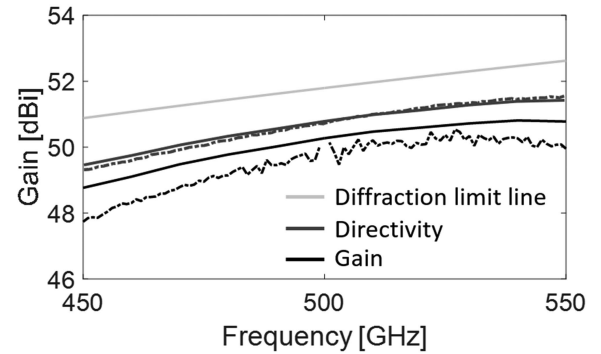
antennas are not placed perfectly parallel, a phase coupling error will be committed in the measurement. Another potential source of discrepancy might be dielectric losses in the Parylene-C coating [34], which were considered to be lossless in the simulations.

By rearranging the terms in (2), the aperture efficiency, and thereafter lens antenna gain, can be extracted. In this de-embedding, we use the measured near-field distribution shown in Fig. 14 to calculate the amplitude tapering efficiency.³ Moreover, in the de-embedding, it is assumed that the circular-to-rectangular WG transition shown in the inset of Fig. 17 has the same conductivity as extracted from the measurement of the rectangular WG transition, shown in Fig. 17(b). The resulting aperture efficiency is shown in the top of Fig. 19 and is compared with the BoR-MoM simulation. The gain, directly derived from the aperture efficiency and lens aperture area, is also compared in the bottom of Fig. 19 by the black curves, whereas the light gray curve shows the diffraction limit line, i.e., the gain for 100% aperture efficiency. The lens directivity, calculated from the derived lens far-field patterns in Fig. 15, is shown by the dark gray curves and matches well with the simulation. This definition of directivity does not include power that is in spillover of the lens or reflected on the lens surface, since this power is not captured by the near-field measurement. Those terms, together with the return loss, are embedded in the gain curves. The fabricated antenna has an extracted aperture efficiency of 65% and gain of 50 dBi at 500 GHz. A higher aperture efficiency (>70%) can be achieved with the LW stratifications proposed in Section II-B or, ultimately, with an isoflux feed discussed in Section II-A (>80% aperture efficiency).

³Defined as $\eta_{\text{tap}}^{\text{ampl}} = \frac{1}{A_l} \frac{|\iint_S |S_{12}|^2 dS|}{\iint_S |S_{12}|^2 dS}$, where A_l is the lens aperture area.



(a)



(b)

Fig. 19. Lens antenna parameters postprocessed from the coupling measurements. (a) Lens aperture efficiency and (b) gain curve. The solid curves are simulated, whereas the dash-dotted curves are postprocessed from the measurements.

V. CONCLUSION

In this article, a low focal number submm-wave lens antenna is demonstrated that is especially suitable for spectroscopy applications on ultrasmall platforms. The lens antenna, offering 50-dBi gain at 500 GHz, comprises a 74-mm-diameter hyperbolic lens that is placed in a record low-profile position ($f_{\#} = 0.27$, $\theta_0 = 61^\circ$) with respect to a WG feed. Since an OEWG feed would result in an aperture efficiency lower than 60%, the optimal feed pattern is derived by using an antenna-in-reception methodology, which is an isoflux pattern with >80% aperture efficiency. A quasi-analytical optimization of a multilayer LW stratification has been performed, in an attempt to approximate the optimal isoflux pattern. A narrowband (8% fractional) and wideband (20% fractional) designs are proposed, offering aperture efficiencies higher than >70%. As a demonstrator, an example LW lens antenna has been fabricated with silicon micromachining technology and is fully characterized, showing excellent agreement with simulations.

REFERENCES

- [1] P. Siegel, "Terahertz technology," *IEEE Trans. Microw. Theory Techn.*, vol. 50, no. 3, pp. 910–928, Mar. 2002.
- [2] N. Chahat, E. Decrossas, and M. Michael Kobayashi, *Mars Cube One*. New York, NY, USA: Wiley, 2020, ch. 2, pp. 35–89.

- [3] E. Peral et al., "RainCube: The first ever radar measurements from a CubeSat in space," *J. Appl. Remote Sens.*, vol. 13, no. 3, 2019, Art. no. 032504, doi: [10.1117/1.JRS.13.032504](https://doi.org/10.1117/1.JRS.13.032504).
- [4] N. Chahat et al., "Advanced CubeSat antennas for deep space and earth science missions: A review," *IEEE Antennas Propag. Mag.*, vol. 61, no. 5, pp. 37–46, Oct. 2019.
- [5] Z.-W. Miao et al., "A 400-GHz high-gain quartz-based single layered folded reflectarray antenna for terahertz applications," *IEEE Trans. THz Sci. Technol.*, vol. 9, no. 1, pp. 78–88, Jan. 2019.
- [6] Z.-W. Miao et al., "140 GHz high-gain LTCC-integrated transmit-array antenna using a wideband SIW aperture-coupling phase delay structure," *IEEE Trans. Antennas Propag.*, vol. 66, no. 1, pp. 182–190, Jan. 2018.
- [7] D. Kim, J. Hirokawa, M. Ando, J. Takeuchi, and A. Hirata, "64x64-element and 3232-element slot array antennas using double-layer hollow-waveguide corporate-feed in the 120 GHz band," *IEEE Trans. Antennas Propag.*, vol. 62, no. 3, pp. 1507–1512, Mar. 2014.
- [8] N. Chahat, R. E. Hodges, J. Sauder, M. Thomson, and Y. Rahmat-Samii, "The deep-space network telecommunication CubeSat antenna: Using the deployable Ka-band mesh reflector antenna," *IEEE Antennas Propag. Mag.*, vol. 59, no. 2, pp. 31–38, Apr. 2017.
- [9] G. Cortes-Medellin et al., "Optical design for the large balloon reflector," *Proc. SPIE*, vol. 9906, pp. 706–714, 2016, doi: [10.1117/12.2233861](https://doi.org/10.1117/12.2233861).
- [10] M. Alonso-DelPino, P. Goldsmith, C. Elmaleh, T. Reck, and G. Chattopadhyay, "Efficiency optimization of spherical reflectors by feed position adjustments," *IEEE Antennas Wireless Propag. Lett.*, vol. 16, pp. 2865–2868, 2017.
- [11] N. Llombart, G. Chattopadhyay, A. Skalare, and I. Mehdi, "Novel Terahertz antenna based on a silicon lens fed by a leaky wave enhanced waveguide," *IEEE Trans. Antennas Propag.*, vol. 59, no. 6, pp. 2160–2168, Jun. 2011.
- [12] M. Alonso-delPino, S. Bosma, C. Jung-Kubiak, G. Chattopadhyay, and N. Llombart, "Wideband multimode leaky-wave feed for scanning lens-phased array at submillimeter wavelengths," *IEEE Trans. THz Sci. Technol.*, vol. 11, no. 2, pp. 205–217, Feb. 2021.
- [13] S. van Berkel et al., "Wideband double leaky slot lens antennas in CMOS technology at submillimeter wavelengths," *IEEE Trans. THz Sci. Technol.*, vol. 10, no. 5, pp. 540–553, Sep. 2020.
- [14] V. Rumsey, "On the design and performance of feeds for correcting spherical aberration," *IEEE Trans. Antennas Propag.*, vol. 18, no. 3, pp. 343–351, May 1970.
- [15] A. Neto, O. Yurduseven, N. Llombart, and A. Freni, "Antennas in reception," in *Proc. 9th Eur. Conf. Antennas Propag.*, 2015, pp. 1–5.
- [16] A. Freni, N. Llombart, O. Yurduseven, and A. Neto, "On the use of Thevenin circuits in distributed transmission lines and its consequences for antennas in reception," in *Proc. 10th Eur. Conf. Antennas Propag.*, 2016, pp. 1–3.
- [17] M. Arias Campo, D. Blanco, S. Bruni, A. Neto, and N. Llombart, "On the use of Fly's eye lenses with leaky-wave feeds for wideband communications," *IEEE Trans. Antennas Propag.*, vol. 68, no. 4, pp. 2480–2493, Apr. 2020.
- [18] H. Minnett and B. Thomas, "A method of synthesizing radiation patterns with axial symmetry," *IEEE Trans. Antennas Propag.*, vol. AP-14, no. 5, pp. 654–656, Sep. 1966.
- [19] S. Bosma, N. van Rooijen, M. Alonso-delPino, and N. Llombart, "A wideband leaky-wave lens antenna with annular corrugations in the ground plane," *IEEE Antennas Wireless Propag. Lett.*, vol. 21, no. 8, pp. 1649–1653, Aug. 2022.
- [20] S. v. Berkel, M. Alonso-delPino, C. Jung-Kubiak, and G. Chattopadhyay, "Efficient waveguide feeds for low-profile submm-wave lens antennas," in *Proc. 47th Int. Conf. Infrared Millimeter Terahertz Waves*, 2022, pp. 1–2.
- [21] C. A. Balanis, *Antenna Theory: Analysis and Design*. Hoboken, NJ, USA: Wiley, 2015.
- [22] G. Minatti, S. Maci, P. De Vita, A. Freni, and M. Sabbadini, "A circularly-polarized isoflux antenna based on anisotropic metasurface," *IEEE Trans. Antennas Propag.*, vol. 60, no. 11, pp. 4998–5009, Nov. 2012.
- [23] F. Caminita, E. Martini, G. Minatti, M. Sabbadini, and S. Maci, "Low-profile dual-polarized isoflux antennas for space applications," *IEEE Trans. Antennas Propag.*, vol. 69, no. 6, pp. 3204–3213, Jun. 2021.
- [24] X. Ren, S. Liao, and Q. Xue, "A circularly polarized spaceborne antenna with shaped beam for earth coverage applications," *IEEE Trans. Antennas Propag.*, vol. 67, no. 4, pp. 2235–2242, Apr. 2019.
- [25] A. R. Maldonado and M. A. Panduro, "Synthesis of concentric ring antenna array for a wide isoflux pattern," *Int. J. Numer. Model.: Electron. Netw. Devices Fields*, vol. 28, no. 4, pp. 433–441, 2015.
- [26] R. Ravanelli, C. Iannicelli, N. Baldecchi, and F. Franchini, "Multi-objective optimization of an isoflux antenna for Leo satellite down-handling ink," in *Proc. 18th Int. Conf. Microw. Radar Wireless Commun.*, 2010, pp. 1–4.
- [27] A. Neto, N. Llombart, G. Gerini, M. D. Bonnedal, and P. de Maagt, "EBG enhanced feeds for the improvement of the aperture efficiency of reflector antennas," *IEEE Trans. Antennas Propag.*, vol. 55, no. 8, pp. 2185–2193, Aug. 2007.
- [28] D. J. B. Montero, "Leaky waves for near and far field antenna beam shaping," Ph.D. dissertation, Dept. Signal Process., Univ. Carlos III de Madrid, Getafe, Spain, 2014.
- [29] K. Michalski and J. Mosig, "Multilayered media Green's functions in integral equation formulations," *IEEE Trans. Antennas Propag.*, vol. 45, no. 3, pp. 508–519, Mar. 1997.
- [30] M. Qiu, G. Eleftheriades, and M. Hickey, "A reduced surface-wave twin arc-slot antenna element on electrically thick substrates," in *Proc. IEEE Antennas Propag. Soc. Int. Symp.*, 2001, pp. 268–271.
- [31] M. Mrnka and Z. Raida, "An effective permittivity tensor of cylindrically perforated dielectrics," *IEEE Antennas Wireless Propag. Lett.*, vol. 17, no. 1, pp. 66–69, Jan. 2018.
- [32] C. Jung-Kubiak et al., "A multistep DRIE process for complex terahertz waveguide components," *IEEE Trans. THz Sci. Technol.*, vol. 6, no. 5, pp. 690–695, May 2016.
- [33] M. Arias Campo et al., "H-band quartz-silicon leaky-wave lens with air-bridge interconnect to GaAs front-end," *IEEE Trans. THz Sci. Technol.*, vol. 11, no. 3, pp. 297–309, Mar. 2021.
- [34] J. Bueno, S. Bosma, T. Bußkamp-Alda, M. Alonso-delPino, and N. Llombart, "Lossless matching layer for silicon lens arrays at 500 GHz using laser ablated structures," *IEEE Trans. Antennas Propag.*, vol. 12, no. 6, pp. 667–672, Nov. 2022.



Sven van Berkel (Member, IEEE) received the B.Sc. and M.Sc. (*cum laude*) degrees in electrical engineering from the Delft University of Technology (TU Delft), Delft, The Netherlands, in 2012 and 2015, respectively, and the Ph.D. (*cum laude*) degree in electromagnetics from the Delft University of Technology (TU Delft), Delft, in 2020.

During his master's degree, he specialized in telecommunications engineering with a focus on antennas and electromagnetic wave theory. His Ph.D. research was conducted with the Terahertz Sensing Group, TU Delft, and focused on passive imaging systems, ultrawideband antennas for millimeter- and submillimeter-wave applications, quasi-optical systems and analytical/numerical techniques in electromagnetics, and transmission line characterization. From 2020 to 2022, he was a NASA Postdoctoral Program Fellow with the Submillimeter-Wave Advanced Technology Group, NASA Jet Propulsion Laboratory, California Institute of Technology, Pasadena, CA, USA, where he has been a Radio Frequency/Microwave Engineer since July 2022. In this fellowship, he conducted research on wideband, multibeam, and beam-scanning antenna architectures for terahertz spectroscopy instruments.

Dr. van Berkel was the recipient of the Vederprijis 2020, a Dutch award given yearly to a researcher in the field of radio and microwaves, for his Ph.D. research.



Maria Alonso-delPino (Senior Member, IEEE) received the bachelor's degree in telecommunications engineering from the Technical University of Catalonia (UPC), Barcelona, Spain, in 2008, the M.S. degree in electrical engineering from the Illinois Institute of Technology, Chicago, IL, USA, in 2008, and the Ph.D. degree in signal theory and communications/electrical engineering from UPC in 2013.

From 2014 to 2015, she was a Postdoctoral Researcher at the Delft University of Technology (TU Delft), Delft, The Netherlands. From 2015 to 2016, she was a NASA Postdoctoral Fellow at the Jet Propulsion Laboratory, California Institute of Technology, Pasadena, CA, USA, where she was a Member of the Technical Staff with the Submillimeter-Wave Advanced Technology Group of from 2016 to 2020. Since 2020, she has been an Assistant Professor with TU Delft. Her research interests include millimeter- and submillimeter-wave heterodyne and direct detection receiver technologies, antennas, and quasi-optical systems.

Dr. Alonso-delPino was the recipient of the Outstanding Reviewer Award of IEEE TRANSACTIONS ON TERAHERTZ SCIENCE AND TECHNOLOGY in 2013, a corecipient of the 2014 IEEE Terahertz Science and Technology Best Paper Award in 2014, and a corecipient of the European Conference on Antennas and Propagation Best Antenna Design Paper Award in 2022.



Cecile Jung-Kubiak (Senior Member, IEEE) received the M.S. degree in physics and materials chemistry from Polytech Montpellier, Montpellier, France, in 2006, and the Ph.D. degree in physics from Université Paris-Sud XI, Orsay, France, in 2009.

She was the recipient of a two-year NASA Postdoctoral Fellowship with the California Institute of Technology, Pasadena, CA, USA, in 2010. She is currently a Member of the Technical Staff of the Advanced Optical and Electromechanical Microsystems Group, Jet Propulsion Laboratory (JPL), California Institute of Technology. She has coauthored more than 90 papers in international journals and conferences and holds several patents. Her research interests include the development of silicon-based microinstruments, the miniaturization of multipixel arrays at terahertz frequencies, and microelectrospray propulsion systems.

Dr. Jung-Kubiak was a recipient of the 2020 NASA Early Career Public Achievement Medal, the 2018 JPL Lew Allen Award, the 2014 IEEE Terahertz Science and Technology Best Paper Award, and the 2010 JPL Outstanding Postdoctoral Research Award in the field of technology, instrumentation, and engineering.



Goutam Chattopadhyay (Fellow, IEEE) received the Ph.D. degree in electrical engineering from the California Institute of Technology (Caltech), Pasadena, CA, USA, in 2000.

He is currently a Senior Research Scientist with the NASA's Jet Propulsion Laboratory, Caltech, and a Visiting Associate with the Division of Physics, Mathematics, and Astronomy, Caltech. He has authored and coauthored more than 350 publications in international journals and conferences and holds more than 20 patents. His research interests include microwave, millimeter-wave, terahertz receiver systems and radars, and development of space instruments.

Dr. Chattopadhyay is a Fellow of the Institution of Electronics and Telecommunication Engineers (IETE, India) and an IEEE Distinguished Lecturer. He is an elected AdCom Member of the IEEE Microwave Theory and Techniques Society, the Chair of the Membership and Geographic Activities Committee, and the Past Chair of the Meetings and Symposium Committee. He was the recipient of more than 35 NASA technical achievement and new technology invention awards, the IEEE Region 6 Engineer of the Year Award in 2018, and the Distinguished Alumni Award from the Indian Institute of Engineering Science and Technology, India, in 2017. He was also the recipient of the Best Journal Paper Award in 2013 and 2020 by IEEE TRANSACTIONS ON TERAHERTZ SCIENCE AND TECHNOLOGY, the Best Paper Award for Antenna Design and Applications at European Antennas and Propagation Conference in 2017, the IETE Bimani Sen Memorial Award in 2022, and the Prof. S. N. Mitra Memorial Award in 2014.